Graphdiyne Ultrathin Nanosheets for Efficient Water Splitting

Yuxin Liu, Yurui Xue,* Huidi Yu, Lan Hui, Bolong Huang,* and Yuliang Li*

Y. Liu, Prof. Y. Xue, H. Yu, Dr. L. Hui, Prof. Y. Li

Institute of Chemistry, Chinese Academy of SciencesBeijing 100190, P. R. China

E-mail: xueyurui@iccas.ac.cn; ylli@iccas.ac.cn

Prof. Y. Xue

Science Center for Material Creation and Energy ConversionSchool of Chemistry and Chemical Engineering

Institute of Frontier and Interdisciplinary ScienceShandong UniversityJinan 250100, P. R. China

Prof. B. Huang

Department of Applied Biology and Chemical TechnologyThe Hong Kong Polytechnic UniversityHung Hom, Kowloon, Hong Kong SAR, P. R. China

E-mail: bhuang@polyu.edu.hk

Prof. Y. Li

University of Chinese Academy of SciencesBeijing 100049, P. R. China

Abstract:

Graphdiyne (GDY) is an emerging 2D carbon material that exhibits unusual structures and properties. Therefore, growing heterogeneous materials on the surface of GDY is very attractive to achieve efficient energy utilization. Here, a simple method for the controllable synthesis of ultrathin charge-transfer complexes (CTs) of nickel with terephthalic acid nanosheets on GDY is reported. This catalyst shows record-high oxygen evolution reaction (OER) activity with an overpotential of only 155 mV to deliver a current density of 10 mA cm^{-2} in an alkaline electrolyte. Density functional theory calculations reveal that a strong p–d coupling effect in the GDY–CT interface region enhances the overall electronic activity, resulting in fast reversible redox-switching with a low electron-transfer barrier. Experimental characterization confirms that GDY plays a key role in modulating the morphological and electronic structures to accelerate the OER rate. These findings are expected to contribute to the design of more efficient catalysts for the realization of efficient hydrogen energy

technologies.

Introduction

Hydrogen generations by water splitting ($2H_2O \rightarrow 2H_2 + O_2$) provides a green and sustainable way for efficient energy conversion and storage to conquer various challenges to the future of the hydrogen economy (*1-3*). Oxygen evolution reaction (OER) plays a critical role in water splitting by providing required electrons and protons but suffers from the sluggish kinetics and large overpotentials (*4*). Improving the activity and stability of OER catalysts has great significance to make water splitting an efficient and viable technology.

In the past decades, researchers have gained significant advances in developing active materials for OER (*5-11*). However, the state-of-the-art OER catalysts are generally based on noble metals, suffering from high cost and scarcity. In addition, the best current available materials still need large overpotentials over 191 mV to achieve 10 mA cm^{-2} (*7-11*). Therefore, fabricating highly active, stable and low-cost catalysts is a challenging task in this field. Along with the inherent advantages of high electron-transfer and mass transport abilities, and more exposed active sites, the ultrathin 2D metal-organic frameworks (MOFs) have shown promising potential as the efficient catalyst (*9, 12, 13*). In the MOF synthesis process, metal precursors were found as the starting points (*14*). But, the MOFs were conventionally synthesized by mixing of all the reactants metal ions and organic ligands into one pot at elevated temperatures, in which the MOFs grow along all directions simultaneously and it is challenging to control their morphologies. Another major problem is the reported MOF-based electrodes were generally fabricated by adhering MOFs to the substrate using polymeric binders. These remained issues inevitably decrease the catalyst conductivity, mass transport ability, and finally the catalyst activity and stability.

The simple and controllable growth of MOFs with with well-defined chemical and electronic structures on the substrate is able to lead a great advancement for the high-quality synthesis of MOFs and new opportunities for fundamental studies of electrocatalysts.A prerequisite for achieving this goal is to fix metal atoms at substrates to orient growing directions. Graphdiyne (GDY) has shown to be an ideal substrate for anchoring metal atoms (*15-18*) and has been applied in numerous worthwhile applications including catalysis, and energy conversions and storages with remarkable performances (*10, 16-26*). Our previous works showed that metal atoms are favorable to anchor at the corner of the acetylenic rings of GDY firmly and separately (*17, 18*), which supplies the definite starting sites for

MOF growth and guarantees the desired and controllable morphologies. More importantly, the recent advancements in the synthesis of high-quality GDY and GDY-based heterostructure provide a golden opportunity for the fundamental study of OER catalysts, supporting the great potential of the MOF/GDY composite electrocatalyst

Here we report a cost-effective and facile approach for synthesizing ultrathin nickel-MOF nanosheet arrays on GDY (NMNS/GDY), which is highly active for OER in the alkaline electrolyte and displayed a record-high OER performance than all reported catalysts. We applied both theoretical calculations and detailed experimental characterizations to explore the origin of the extremely high activity.

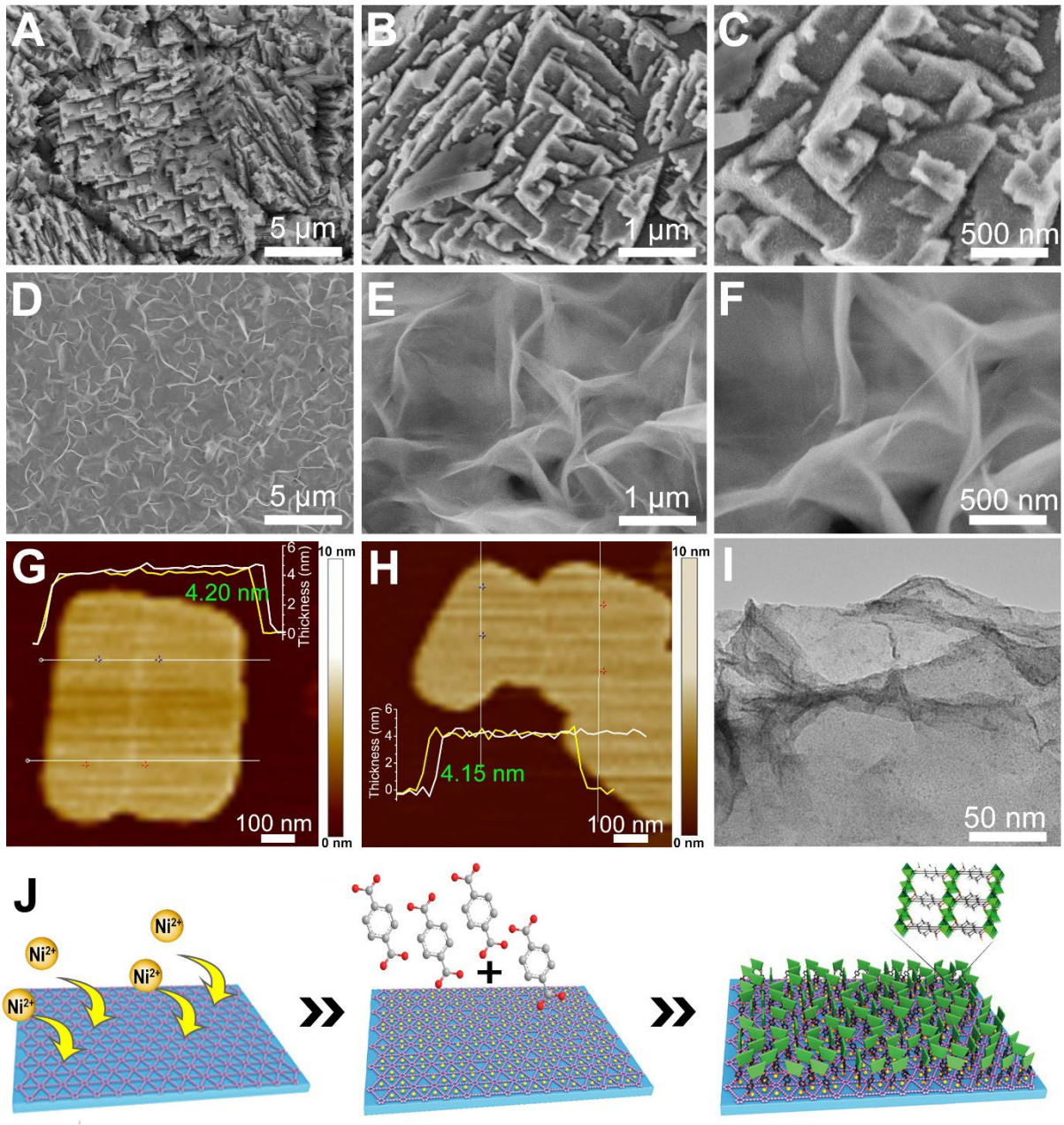

Fig. 1. Morphological characterization. (**A-C**) Low and high magnification SEM images of pristine NiMOF. (**D-F**) Low and high magnification SEM images NMNS/GDY. (**G,H**) AFM images of

ultrathin NiMOF nanosheets grown on GDY with thickness around 4.15~4.20 nm. (**I**) TEM image of ultrathin NiMOF nanosheets grown on GDY. (**J**) The proposed mechanism for the growth of the ultrathin NiMOF nanosheets oriented by GDY, involving the anchoring of the individual metal atoms on GDY and the oriented assembly of MOF nanosheets.

Results and discussion

By using the GDY as the substrate, we successfully synthesized self-supported ultrathin metal MOF nanosheets in a controllable manner. Briefly, a piece of GDY foam (fig. S1) was first immersed in a Ni^{2+} solution for at least two hours, followed by being transferred into a Teflon-autoclave and kept at 120 ℃ for the growth of MOF nanosheets (UMNS/GDY).

Scanning electron microscopy (SEM), transmission electron microscopy (TEM), and atom force microscope (AFM) were used to examine the morphology of the samples. **Figure 1A-C** present the SEM images of NiMOF synthesized directly on Ni foam substrates. The NiMOF shows an irregular rough surface morphology with NiMOF nanoparticles crowded together. By using GDY as the growth substrate, the ultrathin NiMOF nanosheets with 2D morphology were obtained (SEM images: Fig. 1D-F; AFM images: Fig. 1G and 1H; TEM image: Fig. 1I). AFM results reveal that these nanosheets showed the uniform thickness around 4.15 nm (Fig. 1G and 1H). Energy dispersive x-ray spectroscopy (EDS, fig. S2) and the scanning TEM (STEM) elemental mapping measurements (fig. S3) on the MOF nanosheet confirm the uniform distribution of only Ni, C, and O elements in the nanosheetswithout any impurity. These findings all indicate that the GDY plays a key role in the morphological control and oriented the formation of ultrathin MOF nanosheets. According to our previous reports (*15, 17*), metal atoms are inclined to anchor on the surface of GDY. These anchored metal atoms act as the starting points for MOF growth (*13, 14*), which guide the growth along the oriented directions and leads to the formation of ultrathin MOF nanosheets (Fig. 1J). The PXRD patterns showed that the pristine MOF and NMNS/GDY have the same crystal phase (fig. S4). Such a growth approach substantially differs from those conventional ones.

The composition and chemical state of the samples are investigated by x-ray photoelectron spectroscopy (XPS). In the high-resolution C 1s XPS spectra (Fig. 2A), GDY displays four characteristic peaks at 284.5 (sp^2-C), 285.2 (sp-C), 286.9 (C-O), and 288.3 eV (C=O), respectively; while for NMNS/GDY, a new peak at 291.0 eV was observed, which might be resulted from the interaction of MOF and GDY. Compared with pure MOF, *sp*-C peak was observed, indicating the intact of the GDY structure during the MOF growing process. The Ni 2p XPS spectra reveal the coexistence of Ni^{2+}/Ni^{3+} redox couple in NMNS/GDY (Fig. 2B) (*27, 28*). It is observed that NMNS/GDY has a larger Ni^{2+}/Ni^{3+} ratio than that of NiMOF, and the binding energy of NMNS/GDY shifts toward higher binding energy in the Ni 2p spectra (Fig. 2C); in the O 1s spectra (Fig. 2D), the peak at 533.32 eV shifts 0.65 eV to lower binding energy. These indicate the significant charge

transfers between GDY and MOF species (in accordance with the following theoretical results), which is beneficial in improving catalytic activity.

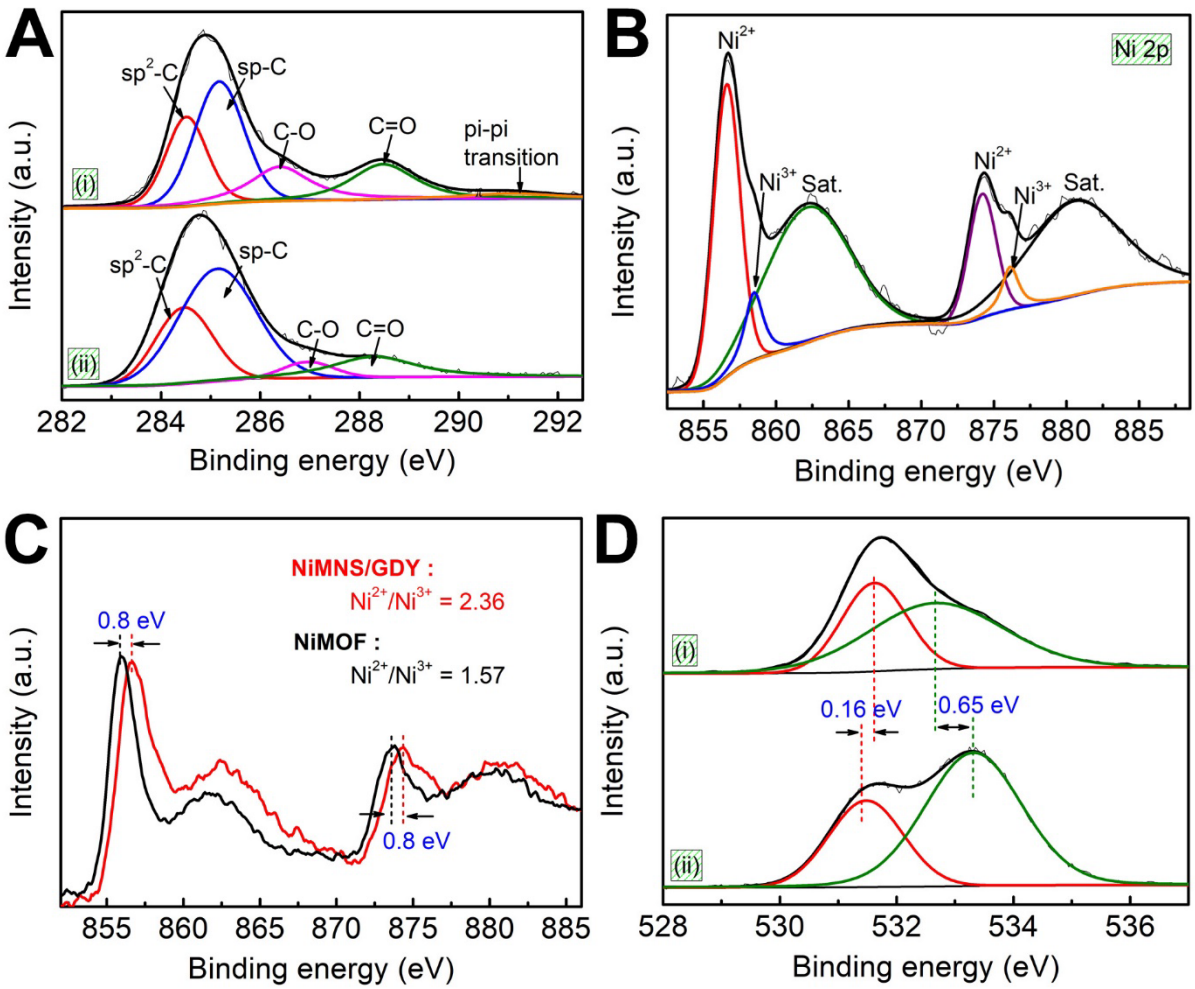

Fig. 2. Structural measurements. (**A**) High-resolution C 1s XPS spectra of (i) NiMNS/GDY and (ii) pure GDY. (**B**) High-resolution Ni 2p XPS spectrum of NiMNS/GDY. (**C**) High-resolution Ni 2p XPS spectra of NiMNS/GDY and NiMOF. (**D**) High-resolution O 1s XPS spectrum of (i) NiMNS/GDY and (ii) NiMOF.

The electronic structural and energetic properties of the NiMNS/GDY were further studied by density functional theory (DFT) calculations. To the best lattice-matching effect, the MOF-(111) surface interfaces with GDY. The fully relaxed the lattice parameters allow the most stable GDY||MOF bonding within an interface distance of 3.3 Å (**Fig. 3A**). The bonding and anti-bonding orbitals near the Fermi level (E_F) demonstrate the electronic distribution on the GDY surface has been evidently modified with an electron-rich character. This derives from the electron-pushing feature contributed from the MOF surface (**Fig. 3B**). From the DFT calculations of the pure GDY system, we found that the p-orbitals remained high and close to the Fermi level (E_F) while the s-orbitals were deep-lying, measured through the projected density of states (PDOSs). This indicates the p-orbitals

are the predominant electronic active component for the three typical C-sites (C1, C2, and C3; **Fig. 3C, inset**). Taking the p-orbitals of C1, C2, and C3 sites, we observed that the overall p-bands for the C1, C2, and C3 sites have been downshifted in a magnitude of 1.0 eV for GDY||MOF. Such electronic difference between pure GDY and GDY||MOF system demonstrates an evident contrast of electronic activities indicating the GDY surface turns to be more electron-rich character towards even higher selectivity of site-to-site electron-transfer onto O-related species (**Fig. 3C**). The PDOSs of O-related species have been demonstrated regarding the OER process, which clearly illustrates the electron-transfer between itinerant H_2O and adsorbing H_2O, as well as the other species. Especially, the electronic contrast between the adsorbing OOH and O=O groups exhibit the substantial strong tendency of H-desorption driven by an efficient reversible electron-transfer (**Fig. 3D**). Considering the contribution of the *p-d* coupling effect, the interface turns out to be the electronic active region. With a comparison between the native MOF (111) surface (**Fig. 3E**) and GDY||MOF interface systems (**Fig. 3F**), the *p-d* coupled electronic transfer within the interfacial region has been further boosted. This arises because the *p-d* overlapping gap has been evidently narrowed from 2.4 eV to 1.0 eV (**Fig. 3E,F**). Therefore, the strongly coupled GDY||MOF interface region plays a dominant role in elevating the active site selectivity on the GDY surface *via* modifying the GDY system towards the more electron-rich character.

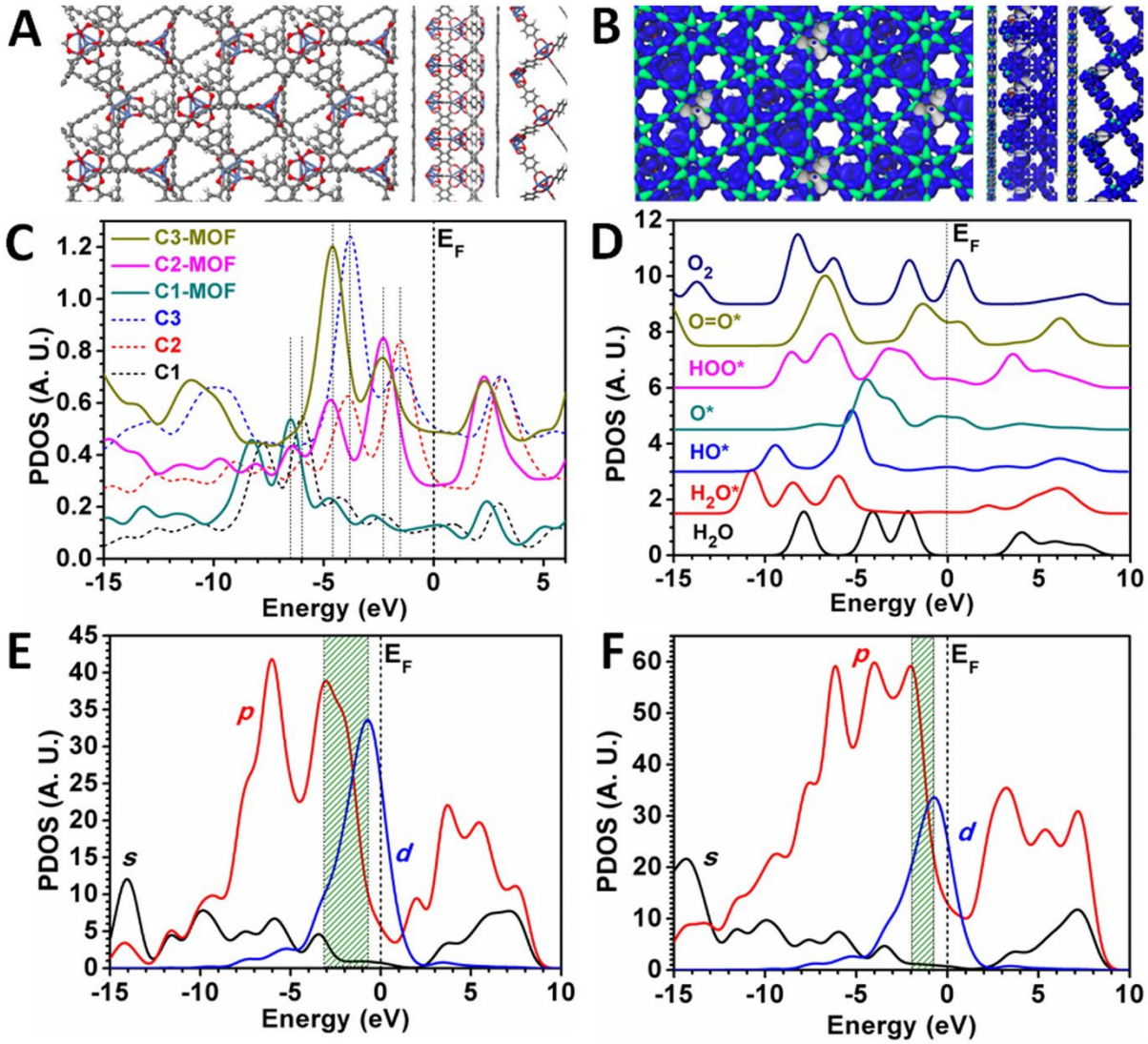

Fig. 3. Electronic structures and activities for OER catalysis. (**A**) The atomic structure of GDY||MOF interface is given within different angles of view (C=grey, O=red, Ni=blue, and H=white.) (**B**) The real spatial contour plots for bonding (blue isosurface) and anti-bonding (green isosurface) orbitals near E_F. (**C**) PDOSs comparison of (C1, C2, and C3) sites between pristine GDY and GDY||MOF interface systems. (**D**) Individual benchmarks of PDOSs of O-related species among initial reactants, intermediates, and final products. (**E**) PDOSs of intrinsic MOF-(111) surface. (**F**) PDOSs of overall GDY||MOF interfacial region. (Green shaded area denotes the p-d overlapping gap.)

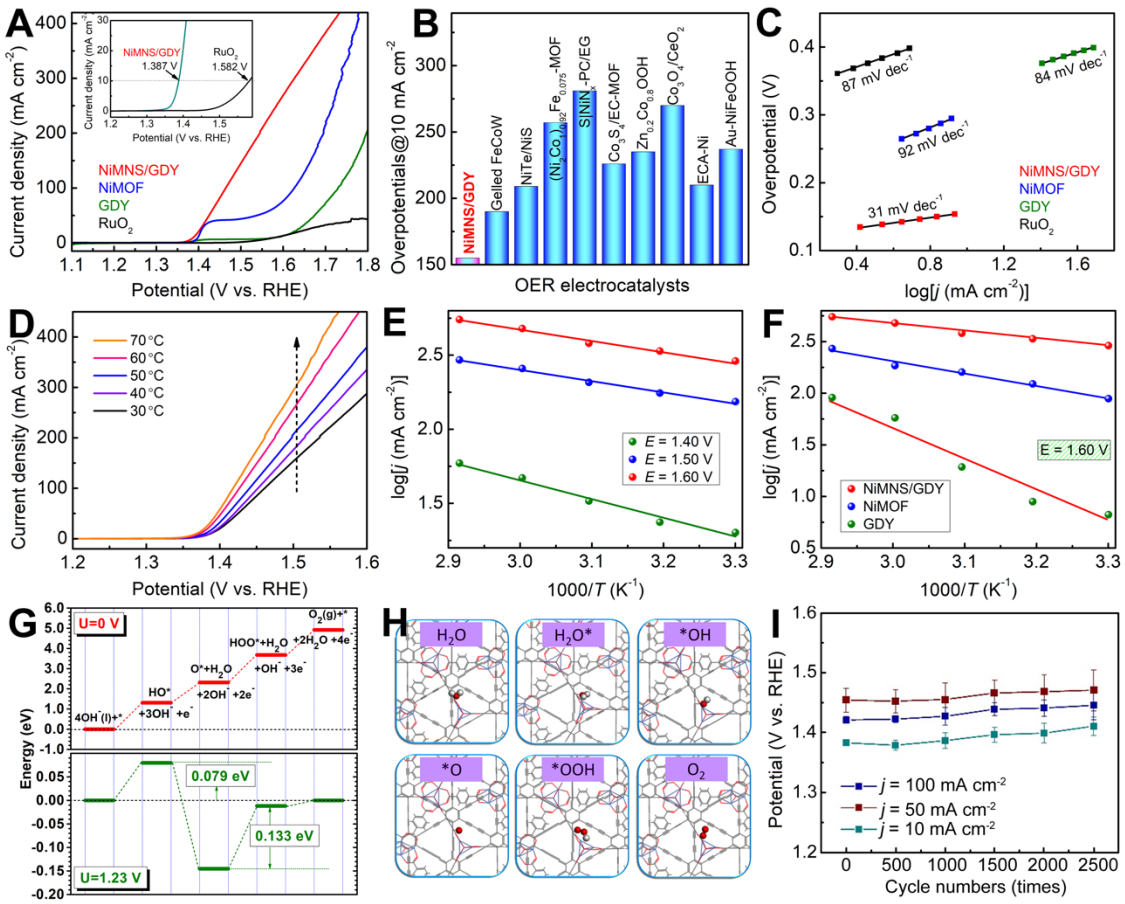

Fig. 4. OER performances. (**A**) Polarization curves of NiMNS/GDY, NiMOF, GDY and RuO_2 in oxygen-saturated 1.0 M KOH (inset: the enlargement of the low overpotential area). (**B**) OER activity comparison of NiMNS/GDY with other catalysts in alkaline solution. (**C**) Tafel plots of the NiMNS/GDY, NiMOF, GDY and RuO_2. (**D**) Polarization curves of NiMNS/GDY recorded at different temperatures. (**E**) Arrhenius plots for OER tested on NiMNS/GDY at different potentials. (**F**) Arrhenius plots for OER tested on NiMNS/GDY, NiMOF and GDY at 1.60 V (vs. RHE). (**G**) OER energetic pathway contributed by the GDY||MOF interface system. (**H**) Structural configuration of different O-species within the OER catalysis process. (**I**) Stability measurements of NiMNS/GDY. The measured overpotentials at 10, 50 and 100 mA cm^{-2}, respectively, during 2500 cycle experiments plotted vs the number of cycles. The error bars show the standard deviation of the measurements.

Representative OER performances of the catalysts were estimated using a typical three-electrode cell at a scan rate of 1.0 mV s^{-1} in O_2-saturated 1.0 M KOH aqueous solution. All polarization curves were corrected by the *iR*-compensation. Remarkably, the NiMOF/GDY needs a record small overpotential of 155 mV to deliver 10 mA cm^{-2} (**Fig. 4A**, all current densities based on the projected geometric area), indicating a significantly enhanced catalytic activity. While the pristine NiMOF and GDY need larger overpotential to achieve the same current density. This value is also much smaller than RuO_2 (350 mV) and the reported state-of-the-art OER catalysts (**Fig. 4B**, table S2), including NiCo-UMOFNs (250 mV) (*9*), G-FeCoW (191 mV) (*8*). **Figure 4C** shows that the Tafel slope of

NiMNS/GDY (31 mV dec^{-1}) is greatly smaller than that of RuO_2 (87 mV dec^{-1}), NiMOF (92 mV dec^{-1}), GDY (84 mV dec^{-1}), suggesting its superior OER kinetics. The excellent catalytic activity of NiMNS/GDY was further verified by its high turnover frequency (TOF) value (please see Method Section for details) (*29*). For instance, at the overpotential of 300 mV, the Ni-MOFNS/GDYF displays a higher TOF value of 1.03 s^{-1} (the lower limit value), much larger than NiMOF (0.3 s^{-1}).

To gain more insights into the origin of such high activity, the Brunauer-Emmett-Teller (BET) surface area, electrochemically active surface area (ECSA), and electrochemical impedance spectroscopy (EIS) were performed. The BET results (fig. S5) showed that the surface area of NiMNS/GDY is 36.60 m^2 which is 1.5 times than pure NiMOF (24.26 m^2), in accordance with the electrochemical measurements that the NiMNS/GDY had a larger ECSA than pure NiMOF (fig. S6). This confirmed the presence of more active sites for the ultrathin MOF nanosheets grown on GDY than NiMOF. To study the charge transfer behavior of the catalysts, EIS Nyquist plots were recorded (fig. S7) and fitted using a $R_s(Q(R_{ct}(Q\ R_{ad}))$ two-time constant parallel (2TP) equivalent circuit model (R_s: solution resistance; R_{ct}: charge transfer resistance; R_{ad}: adsorption resistance; table S3). NiMNS/GDY exhibits the smallest values of R_s (0.66 Ω) and R_{ct} (5.02 Ω) than pure NiMOF (R_s = 3.05 Ω; R_{ct} = 68.17 Ω) and GDY (R_s = 2.76 Ω; R_{ct} = 103.4 Ω), indicating the fastest charge transfer of NiMNS/GDY for OER. The smallest absorption resistance of NiMNS/GDY implies the easiest OER intermediates absorption on its surface, which facilitates the reaction process.

The reaction rate was estimated by calculating the activation energies through the Arrhenius equation. It was found that, at the same applied potentials, NiMNS/GDY exhibited larger catalytic activities at higher temperatures (**Fig. 4D**). With the potentials increased from 1.40 to 1.50, and 1.60 V (v. RHE), the activation energies decreased from 29.77 to 16.45, and 15.20 kJ mol^{-1}, respectively (**Fig. 4E**, and table S4). In addition, the Arrhenius plots at 1.60 V (**Fig. 4F**) reveals that NiMNS/GDY has a lower reaction barrier of 15.20 kJ mol^{-1} than pure NiMOF (22.28 kJ mol^{-1}) and GDY (80.86 kJ mol^{-1}). The OER pathway shows that the system is an energetically favorable catalyst under U=0 and U=1.23 V respectively with substantially low barriers (**Fig. 4G**). The initial barrier of capturing of the itinerant OH group results in an increase in energy of 1.31 eV (U=0 V), implying the initiation is very reactive at a low overpotential. The bonding preference of GDY-O* leads to an ideal position (2.31 eV, U=0 V) for the potential determining step of forming *OOH (3.68 eV, U=0 V). Meanwhile, the final $[HOO^*+OH^-+H_2O+3e^-] \rightarrow [O_2+2H_2O+4e^-]$ transformation is also active with a rather minor uphill barrier of 1.24 eV at U=0 V. Compared the pathway at U=1.23 V, we confirm the overall overpotential (i.e. η = max[(barrier-1.23 eV)/e]=0.133 V) is highly close to the experimentally measured 0.159 V. This indicates an essential consistency between theoretical analysis and experimental observation. Therefore, the GDY||MOF system achieves a very high OER performance supported by a nearly barrier-free water splitting process. From the view of the local structural

configuration (**Fig. 4H**), it shows that the H_2O can be uniquely stabilized at the linkage of GDY along (C1-C2-C3-C2-C1), while the OH, O, as well as the OOH groups are further stabilized within the region between C2 and C3 sites. We confirm that the (C2, C3)-site is electronically active to locally splitting H_2O for efficient OER process. The preeminent electron-exchange and transfer (EXT) capability are predominantly supported by the strongly coupled interfacial active region. As a result of these geometric and electronic changes, we identified a favorable direct O_2 mechanism for OER with a theoretical overpotential of only 0.4 V compared with the standard electrochemical OOH mechanism [computational methodology details are provided in (19)].

Long-term stability is an important criterion for practical applications (*30*). The stability of NiMNS/GDY was first assessed by using continuous cyclic voltammetry (CV) method for 2500 cycles. The overpotentials of every 500 cycles at 10, 50, and 100 mA cm^{-2}, respectively, for at least three independent experiments, were shown in **Figure 4I**. There was negligible decrease in catalytic activities. Besides, the catalytic activity could be maintained over 90 hours during the continuous electrolysis in 1.0 M KOH electrolyte (fig. S8), revealing the robust long-term stability of NiMNS/GDY.

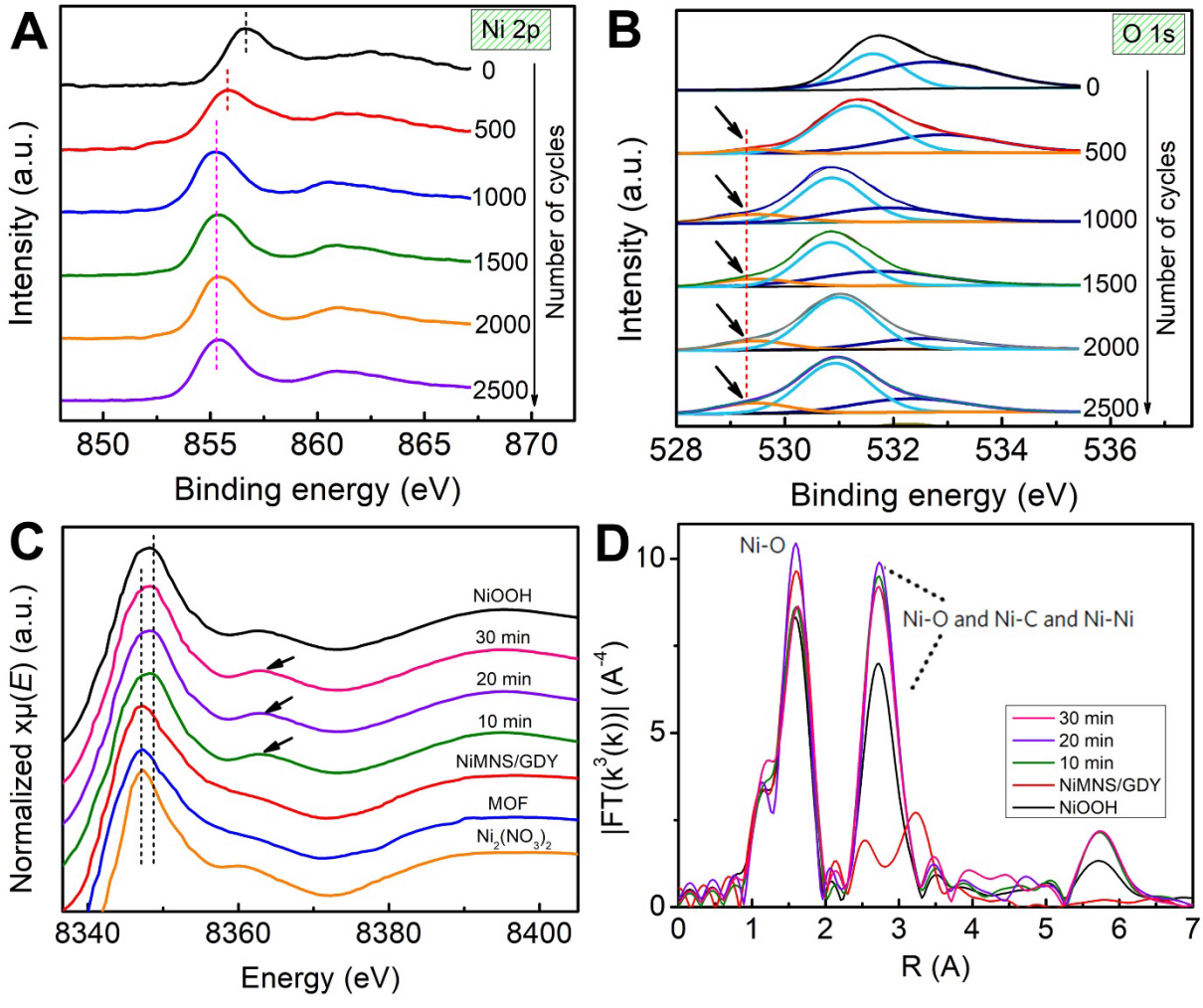

Fig. 5. Structural evolution during the electrocatalysis.

XPS and the X-ray absorption spectroscopy (XAS) were performed to identify the structural evolution of the catalyst during the continuous cycling tests. **Figure 5** shows the C 1s, the Ni 2p3/2, and the O 1s XPS spectra of the fresh-synthesized NiMNS/GDY as well as the ones obtained after different cycling tests. It was observed that there are almost no changes in the C 1s spectra (fig. S9), indicating the chemical structures of GDY and organic ligands are maintained well during the continuous electrocatalysis. In the case of the O 1s XPS spectra, the peaks at the BE above 532 eV correspond to the organic C=O bonds. The peaks at 531~531.8 eV correspond to the surface excess oxygen or hydroxide species. The new peaks positioned at 529.3 eV for all samples after the cycling tests might be ascribed from the lattice oxygen of metal oxide species. The Ni 2p photoelectron peaks were shown in Fig. 5A, substantial changes in the spectra were observed. The Ni $2p_{3/2}$ positions move from 856.6 eV (freshly-synthesized sample) to 855.9 eV (500-cycling-test sample) and to 855.2 eV (other cycling-test samples), respectively. The change of the binding energy indicates the substantial change of the oxidation state. Previous studies (*27, 28*) reported that the binding energies of 855.3 eV corresponded to the $Ni(OH)_2$ phase and 855.8 eV corresponded to the NiOOH phase. Obviously, the proportion of Ni^{2+} species increases with the proceeding of the electrocatalysis. Our electrochemical measurements already showed that the OER catalytic activities have slightly decreased with increasing cycling cycles. Therefore, it is easy to get a conclusion that the mixed Ni^{2+}/Ni^{3+} species endows the catalyst with high activity, but, there would be a decrease in the catalytic activity with the increase of the proportion of Ni^{2+} species.

We further investigated the effects of the incorporating of GDY on the electronic and coordination nature of Ni by X-ray absorption spectroscopy (XAS). We examined the Ni-MOFNS/GDY and pure Ni-MOF samples. The extended X-ray absorption fine structure (EXAFS) spectra and the fitted parameters are summarized. While the dominant peak at 1.60 Å is assigned to the first shell coordination of M (metal)–O, the relatively weak peaks at 2.35, 2.86 and 3.24 Å are associated with higher shell contributions in M–C, M–O and M–M, respectively. Compared to bulk NiMOFs, the average coordination number of the M–C or M–O shell in all NiMOF/GDY exhibits an obvious and identical decrease. This clearly reveals the existence of coordinatively unsaturated metal sites on Ni-MOF/GDYF surfaces, which can lead to enhanced catalytic activity. Moreover, in situ XAS spectra measurements were performed to understanding the nature of the catalytic active sites of NiMNS/GDY (**Fig. 5**). The normalized Ni K-edge XANES spectra are shown in Fig. 5a. The main Ni K-edge peaks of freshly-prepared NiMNS/GDY and $Ni(NO_3)_2$ are centered at the similar energies (8347.0 eV), implying the similar valence states of Ni species. It is found that the Ni K-edge peak of

NiMNS/GDY moves to higher energy (8348.0 eV) in the OER catalysis process, indicating the oxidation of Ni atoms during the electrocatalysis. This reveals the phase transition in the NiMNS/GDY sample in the OER process.

Conclusion

In summary, by using GDY as substrates, the ultrathin MOF nanosheets array is successfully prepared in situ based on the simple and highly controllable approach. Owing to the superior morphological and electronic properties, the obtained NiMNS/GDY exhibits the ultra-low overpotential of 155 mV for durable OER in basic electrolytes, allowing them to be the promising OER electrocatalysts. DFT calculations reveal that the catalyst possesses an extra-low electron-transfer barrier actualized by a strong p-d coupling effect. The enriched electronic-distribution on the GDY surface not only elevates the fast reversible redox-switching capability but also enhances the site-selectivity by electron-rich character. This is a keyto optimally minimizing the overall OER barrier. This work paves the avenuesfor future catalyst design and optimization, accelerating their applications into the realm of renewable energy technologies for sustainable energy conversion or storage.

References and Notes:

1. J. Luo *et al.*, Water photolysis at 12.3% efficiency via perovskite photovoltaics and earth-abundant catalysts. *Science* **345**, 1593-1596 (2014).
2. M. G. Walter *et al.*, Solar Water Splitting Cells. *Chem. Rev.* **110**, 6446-6473 (2010).
3. S. J. Davis *et al.*, Net-zero emissions energy systems. *Science* **360**, eaas9793 (2018).
4. Z. W. Seh *et al.*, Combining theory and experiment in electrocatalysis: Insights into materials design. *Science* **355**, eaad4998 (2017).
5. J. Suntivich, K. J. May, H. A. Gasteiger, J. B. Goodenough, Y. Shao-Horn, A Perovskite Oxide Optimized for Oxygen Evolution Catalysis from Molecular Orbital Principles. *Science* **334**, 1383-1385 (2011).
6. J. Hwang *et al.*, Perovskites in catalysis and electrocatalysis. *Science* **358**, 751-756 (2017).
7. L. C. Seitz *et al.*, A highly active and stable $IrO_x/SrIrO_3$ catalyst for the oxygen evolution reaction. *Science* **353**, 1011-1014 (2016).
8. B. Zhang *et al.*, Homogeneously Dispersed, Multimetal Oxygen-Evolving Catalysts. *Science* **352**, 333-337 (2016).
9. S. Zhao *et al.*, Ultrathin metal–organic framework nanosheets for electrocatalytic oxygen evolution. *Nat. Energy* **1**, 16184 (2016).
10. L. Hui *et al.*, Overall water splitting by graphdiyne-exfoliated and -sandwiched layered double-

hydroxide nanosheet arrays. *Nat. Commun.* **9**, 5309 (2018).

11. N.-T. Suen *et al.*, Electrocatalysis for the oxygen evolution reaction: recent development and future perspectives. *Chem. Soc. Rev.* **46**, 337-365 (2017).
12. H. Furukawa, K. E. Cordova, M. O'Keeffe, O. M. Yaghi, The Chemistry and Applications of Metal-Organic Frameworks. *Science* **341**, 1230444 (2013).
13. A. J. Howarth *et al.*, Chemical, thermal and mechanical stabilities of metal–organic frameworks. *Nat. Rev. Mater.* **1**, 15018 (2016).
14. O. Shekhah, H. Wang, D. Zacher, R. A. Fischer, C. Wöll, Growth Mechanism of Metal–Organic Frameworks: Insights into the Nucleation by Employing a Step-by-Step Route. *Angew. Chem. In. Ed.* **48**, 5038-5041 (2009).
15. J. J. He *et al.*, Magnetic Properties of Single Transition-Metal Atom Absorbed Graphdiyne and Graphyne Sheet from DFT + U Calculations. *J. Phys. Chem. C* **116**, 26313-26321 (2012).
16. G. Li *et al.*, Architecture of graphdiyne nanoscale films. *Chem. Commun.* **46**, 3256-3258 (2010).
17. Y. Xue *et al.*, Anchoring zero valence single atoms of nickel and iron on graphdiyne for hydrogen evolution. *Nat. Commun.* **9**, 1460 (2018).
18. L. Hui *et al.*, Highly Efficient and Selective Generation of Ammonia and Hydrogen on a Graphdiyne-Based Catalyst. *J. Am. Chem. Soc.* **141**, 10677-10683 (2019).
19. Y. J. Li, L. Xu, H. B. Liu, Y. L. Li, Graphdiyne and graphyne: from theoretical predictions to practical construction. *Chem. Soc. Rev.* **43**, 2572-2586 (2014).
20. C. Huang *et al.*, Progress in Research into 2D Graphdiyne-Based Materials. *Chem. Rev.* **118**, 7744-7803 (2018).
21. X. Gao, H. Liu, D. Wang, J. Zhang, Graphdiyne: synthesis, properties, and applications. *Chem. Soc. Rev.* **48**, 908-936 (2019).
22. Z. Zuo, Y. Li, Emerging Electrochemical Energy Applications of Graphdiyne. *Joule* **3**, 899-903 (2019).
23. Y. Zhao *et al.*, Few-layer graphdiyne doped with sp-hybridized nitrogen atoms at acetylenic sites for oxygen reduction electrocatalysis. *Nat. Chem.* **10**, 924-931 (2018).
24. J. He *et al.*, Hydrogen substituted graphdiyne as carbon-rich flexible electrode for lithium and sodium ion batteries. *Nat. Commun.* **8**, 1172 (2017).
25. W. Ning *et al.*, Synthesis and Electronic Structure of Boron-Graphdiyne with an sp-Hybridized Carbon Skeleton and Its Application in Sodium Storage. *Angew. Chem. Int. Ed.* **57**, 3968-3973

(2018).

26. H. Yu *et al.*, Efficient Hydrogen Production on a 3D Flexible Heterojunction Material. *Adv. Mater.* **30**, 1707082 (2018).
27. N. Weidler *et al.*, X-ray Photoelectron Spectroscopic Investigation of Plasma-Enhanced Chemical Vapor Deposited NiOx, NiOx(OH)y, and CoNiOx(OH)y: Influence of the Chemical Composition on the Catalytic Activity for the Oxygen Evolution Reaction. *J. Phys. Chem. C* **121**, 6455-6463 (2017).
28. A. P. Grosvenor, M. C. Biesinger, R. S. C. Smart, N. S. McIntyre, New interpretations of XPS spectra of nickel metal and oxides. *Surf. Sci.* **600**, 1771–1779 (2006).
29. C. C. L. McCrory, S. Jung, J. C. Peters, T. F. Jaramillo, Benchmarking Heterogeneous Electrocatalysts for the Oxygen Evolution Reaction. *J. Am. Chem. Soc.* **135**, 16977-16987 (2013).
30. Q. Wei *et al.*, Facile one-step synthesis of mesoporous Ni-Mg-Al catalyst for syngas production using coupled methane reforming process. *Fuel* **211**, 1-10 (2018).